Original Research Article

Investigation of 2D anti-scatter grid implementation in a gantry-mounted cone beam computed tomography system for proton therapy

Uttam Pyakurel [a,*], Yawei Zhang [b], Ryan Sabounchi [a], Farhang Bayat [a], Sébastien Brousmiche [c], Curtis Bryant [b], Nancy Mendenhall [b], Perry Johnson [b], Cem Altunbas [a,*]

[a] Department of Radiation Oncology, University of Colorado School of Medicine, 1665 Aurora Court, Suite 1032, Mail stop F-706, Aurora, CO 80045, USA
[b] University of Florida Health Proton Therapy Institute, 2015 N Jefferson St, Jacksonville, FL 32206, USA
[c] Ion Beam Applications, 3 Chemin du Cyclotron, 1348 Louvain-la-Neuve, Belgium

ABSTRACT

Background and purpose: Robust scatter mitigation by 2D anti-scatter grids (2D-ASG) in proton therapy cone beam computed tomography (CBCT) may improve target visualization and computed tomography (CT) number fidelity, allowing online dose verifications and plan adaptations. However, grid artifact-free implementation of 2D-ASG depends on the CBCT system characteristics. Thus, we investigated the feasibility of 2D-ASG implementation in a proton therapy gantry-mounted CBCT system and evaluated its impact on image quality.
Materials and methods: A prototype 2D-ASG and a grid support platform were developed for a proton therapy CBCT system with a 340 cm source to imager distance. The effect of gantry flex on 2D-ASG's wall shadows and scan-to-scan reproducibility of 2D-ASG's wall shadows were evaluated. Experiments were conducted to assess 2D-ASG's wall shadow suppression and the effect of 2D-ASG on image quality.
Results: While maximum displacement in 2D-ASG wall shadows was 103 μm during gantry rotation, the drift from baseline over 3 months was 8 μm and 1 μm in the transverse and axial directions. 2D-ASG shadows were successfully suppressed in CBCT images. With 2D-ASG, maximum Hounsfield Unit (HU) nonuniformity decreased from 134 to 45 HU, contrast-to-noise ratio (CNR) increased by a factor of 2.5, and HU errors were reduced from 34 % to 5 %.
Conclusions: Proton therapy gantry flex was highly reproducible and did not noticeably affect 2D-ASG wall shadow suppression in CBCT images, supporting its feasibility in proton therapy CBCT system. Improved CT accuracy and artifact reduction with 2D-ASG could enhance CBCT-based proton therapy dose calculations.

1. Introduction

Besides accurate target localization, a potential role of cone beam computed tomography (CBCT) in image-guided proton therapy (IGPT) is dose delivery verification and treatment plan adaptations during treatment delivery sessions. Inter-fraction changes in the patient's body habitus and organ positions may alter the proton range, leading to suboptimal dosimetric coverage of targets and compromising normal tissue sparing. Such variations in the proton range and its associated dosimetric impact can be quantified by recalculating the dose using CBCT images. When needed, plans can be modified using CBCT images, rather than planning computed tomography (CT), to deliver the planned dose to targets. Therefore, enhanced CBCT image quality could transform CBCT's utility in IGPT, potentially improving treatment outcomes.

However, CBCT-based proton therapy dose adaptations require high HU accuracy. Insufficient HU accuracy in CBCT often creates a barrier to CBCT-based proton therapy dose calculations. To address this problem, previous works investigated deformable planning CT − CBCT registration methods [1–5]. Such approaches improved dose calculation accuracy but require highly accurate and reliable deformable registration methods. Another approach is software-based scatter correction [6–10] to improve HU accuracy and dose calculations [11–13]. Hardware based scatter mitigation were also investigated, such as bow tie filters [14,15], beam stops, primary modulators [16–18], air gaps [19], and radiographic 1D anti-scatter grid (ASG) [20,21].

The 2D-ASG is another approach for scatter rejection, which provides a factor of 3 to 6 lower scatter to primary ratio than 1D-ASGs. Average primary transmission of a 2D-ASG can reach above 80 % when

compared to 70 % primary transmission by 1D-ASGs [22,23]. In addition, the 2D-ASG enables implementation of the Grid-based Scatter Sampling (GSS) method, which corrects the remaining scatter that is not rejected by the 2D-ASG [24,25]. Prior studies have shown that the 2D-ASG and the GSS approach yields substantially improved image quality compared to 1D-ASGs in CBCT [26–30].

In this work, a 2D-ASG approach was investigated to mitigate scattered radiation in the context of proton gantry-mounted CBCT systems. The design of the 2D-ASG for the proton therapy CBCT aims to meet three goals: robust scatter suppression, high primary transmission, and suppression of 2D-ASG's footprint or wall shadows. Primary and scatter transmission performance mainly depends on 2D-ASG's physical characteristics, system geometry, and properties of the imaged object [23]. Meanwhile, the suppression of 2D-ASG's wall shadows depends on one more major factor: the gantry flex characteristics of the CBCT system [31]. Gantry flex refers to the change in X-ray focal spot and detector positions with respect to each other during the rotation of a CBCT gantry due to the effects of gravity and the design properties of the gantry. When a 2D-ASG is installed on the flat panel detector (FPD), its grid walls cast a shadow, or footprint, on the FPD's pixels. The gantry flex may change the characteristics of the 2D-ASG's wall shadows due to the relative shift in the focal spot position. If such changes in grid wall shadows are not accounted for, 2D-ASG may introduce image artifacts and make 2D-ASG implementation infeasible.

Thus, in this work, the implementation feasibility of 2D-ASG in a proton therapy gantry-mounted CBCT system was investigated for the first time. Specifically, the effect of gantry flex on the 2D-ASG's wall shadows, the reproducibility of wall shadows over time, and the efficacy of wall shadow suppression were investigated. Finally, the effect of scatter mitigation by the 2D-ASG on the CBCT image quality metrics was studied.

2. Materials and methods

2.1. 2D-ASG implementation in proton gantry CBCT system

A 2D-ASG prototype was developed for a gantry-mounted CBCT system (Proteus Plus, IBA, Belgium) at the University of Florida Health Proton Therapy Institute. The CBCT system had a 340 cm source-to-imager distance (SID), where the X-ray source is mounted on the gantry frame, and the FPD is mounted on a retractable electro-mechanical arm. The 2D-ASG was developed and additively manufactured from tungsten. The prototype consists of two grid modules. Each module has a width of 2.7 cm and a length of 20 cm. They were merged to form a 40 cm long 2D-ASG. Selection of 2D-ASG's properties were based on the experience gained in prior studies. The prototype has a grid ratio of 11 and a septal thickness of 0.1 mm. Higher grid ratios accentuate the effect of gantry flex on the grid wall shadows. A grid pitch of 1.6 mm was chosen to correct residual scatter by using the Grid-based Scatter Sampling method. The FPD in the CBCT system has a pixel of 0.296 and 0.444 mm in 2×2 and 3×3 binning modes and the active area is 426×426 mm^2. A 1.6 mm 2D-ASG grid pitch ensures effective residual scatter correction in both binning modes. Selecting a larger grid pitch increases grid height for a given grid ratio, amplifying the effects of gantry flex on grid shadows for only small gains in primary transmission [31].

In addition, a new 2D-ASG mounting platform was developed to install the 2D-ASG onto the FPD. Because the FPD is not designed to implement the 2D-ASG, the new platform allowed retrofitting the 2D-ASG to the existing FPD hardware and electro-mechanical arm without altering the clinical configuration of the CBCT system, finite element analysis (FEA) was conducted to optimize the mounting platform's design to keep it light and, at the same time, minimize distortions due to gravity during gantry rotation.

Primary transmission and 2D-ASG wall shadows of the 2D-ASG assembly were characterized experimentally. For the optimal alignment of

the 2D-ASG septa towards the source, 2D-ASG positioning was adjusted to maximize the primary transmission. Subsequently, changes in grid wall shadows as a function of gantry angle were evaluated by employing the Oversampled Signal Profile (OSP) method in flood CBCT scans acquired without a phantom [31]. Detector pixels undersample the high-gradient signal profile in grid wall shadows due to their relatively large pitch. Hence, the OSP method synthesizes an oversampled signal profile of a grid wall shadow by combining the signal profiles from multiple grid wall shadows, as illustrated in Fig. 2. After the generation of OSPs, a Gaussian curve was fitted to each OSP in each projection. Amplitude, width (two times the standard deviation of the Gaussian fit), and minimum position were extracted from each OSP. The change in shape and position of OSPs were then characterized as a function of gantry angle. Grid wall shadow characterization was done twice, with a three-month gap between the two experiments to assess the changes in 2D-ASG wall shadow characteristics over time. Grid wall shadow characteristics were calculated at different locations across the 2D-ASG for vertical and horizontal grid wall shadows.

To evaluate image quality, CBCT imaging experiments were performed with three different phantoms: Catphan 600 (Phantom Laboratory, NY, USA), Catphan 600 with the outer annulus with 38 cm lateral and 30 cm anterior-posterior separation, and the pelvis phantom (Brainlab AG, Munich, Germany). Two CBCT scans were acquired for each phantom setup, one without and one with the 2D-ASG, and using image acquisition parameters. 470 projections were taken on a full scan geometry at 120 kVp and an exposure of 12.5 ms at 320 mA per projection. Computed Tomography Dose Index (CTDI) was 10.89 mGy per scan. Residual scatter transmitted through the 2D-ASG was corrected by adapting the Grid-based scatter sampling (GSS) method in CBCT scans acquired with the 2D-ASG [24,32]. Combination 2D-ASG and residual scatter correction was referred to as grid-based scatter mitigation in the rest of the text. CBCT scans without 2D-ASG were processed in two different ways, one without scatter correction, and the other with scatter correction by the clinical software package; AdaptInsight 2.1 (IBA) with scatter correction. Such scatter correction was referred to as clinical software correction in the next sections. All images were reconstructed by using the Feldkamp Davis Kress (FDK) algorithm of the circular cone beam reconstruction toolkit (RTK) module, based on the open-source Insight Toolkit (ITK 5.3.0) [33]. All CBCT images were reconstructed with the same voxel size ($0.66 \times 0.66 \times 2.00$ mm^3).

2.2. Characterization of image quality

Suboptimal suppression of 2D-ASG's wall shadows due to gantry flex leads to ring artifacts in CBCT images. Because wall shadows characterized in the flat field calibration data would not perfectly match the characteristics of wall shadows in phantom CBCT scans. Hence, phantom CBCT images were first visually evaluated for ring artifacts.

The HU values of the Catphan material inserts were measured in the CBCT images without scatter mitigation, correction with the clinical software, and with the 2D-ASG coupled with grid-based scatter correction. Measured HU values were compared to the reference values [34]. HU accuracy was evaluated by calculating HU loss, K_{HU}. HU nonuniformity was assessed by placing multiple ROIs in the uniform material sections of phantoms. The HU nonuniformity is expressed as follows:

$$HUnonuniformity(i) = HU(i) - mean(HU) \qquad (1)$$

where $HU(i)$ is the mean value of the ith ROI and $mean(HU)$ is the ensemble average of mean HU values.

The contrast-to-noise ratio (CNR) was also calculated for the Delrin of the Catphan material inserts module.

K_{HU} was assessed by examining the variation in HU values between the small and large Catphan phantoms because object size affects scatter fluence.

$$K_{HU}(\%) = \frac{ROIofHUsmall - ROIofHULarge}{ROIofHUsmall + 1000} \times 100 \qquad (2)$$

The K_{HU} was calculated for Delrin, LDPE, Polystyrene, and Teflon, from 5 axial slices in each CBCT set.

3. Results

As shown in Fig. 1, the 2D-ASG assembly integrated with the grid mounting platform was bolted onto the support arms on the top and bottom sides of the FPD. The grid platform weighs 450 g, maintaining a maximum deflection of less than 30 μm during gantry rotation based on the Finite Element analysis (Supplementary Fig. S1).

At the optimally aligned position, the cumulative primary transmission histograms (PTHs) were generated (Supplementary Fig. S2). The average primary transmission was 83 ± 2 %. The percentage of the pixels that received at least 80 % (PT_{80}) and 50 % (PT_{50}) primary transmission was 65.9 ± 0.3 % and 97.5 ± 0.2 %, respectively.

Generation of the OSP was demonstrated in Fig. 2. Pixel values of five adjacent vertical grid wall shadows were extracted using the pixel profile indicated by the red line. After reordering the pixels, the OSP was generated, and its shape was characterized by a Gaussian-based curve fit. This process was repeated for the horizontal grid wall shadows in each projection.

The amplitude of OSP varied slowly as a function of gantry angle (Fig. 3), and the maximum variation was 5.3 % of the mean amplitude among horizontal and vertical grid walls. Likewise, the mean width of OSP was 335 μm varied a maximum of 5.6 % as a function of gantry angle. OSP amplitudes and widths were similar in two measurements performed three months apart. The most noticeable change was the shift of wall shadow, or OSP, positions as a function of gantry angle.

Maximum shifts in horizontal and vertical grid wall shadows were 103 and 13 μm, respectively, during a CBCT scan. However, OSP shifts as a function of gantry angle were highly repeatable in two measurements performed 3 months apart. At any given gantry angle, the maximum difference between the measurements was 7.1 and 0.9 μm for horizontal and vertical grid walls, respectively. OSPs generated in different neighborhoods across the 2D-ASG exhibited similar characteristics.

Cupping artifacts were significantly reduced with the clinical software correction and were further reduced with the implementation of the 2D-ASG (Fig. 4). The visibility of the structures has been improved, and line profiles demonstrate the reduction in HU nonuniformity (Supplementary Fig. S3). Maximum HU nonuniformity for Catphan large was reduced from 92 HU without scatter correction to 42 HU with the 2D-ASG (Fig. 5a). Similarly, HU nonuniformity decreased from 77 to 15 HU in Catphan small and from 134 to 45 HU in Pelvis phantom images, with scatter mitigation using the 2D-ASG (Fig. 5b, 5c). K_{HU} was up

to 34 ± 0.4 % without scatter mitigation. It was reduced to 8.1 ± 1.2 % and 5 ± 1.7 % with the clinical software correction and grid-based scatter mitigation, respectively (Supplementary Fig. S4).

CNR improvement followed similar trends. For the Catphan large phantom, CNR was 1.5 ± 0.4, 2.2 ± 0.2, and 3.2 ± 0.5 without scatter correction, with the clinical software correction and with the 2D- ASG, respectively. For the small phantom, the CNR was 2.8 ± 0.22, 5.8 ± 0.66, 7.0 ± 0.47, without scatter correction, with clinical software correction, and grid-based scatter mitigation, respectively. The CNR was improved by a factor of 2.5 and 2.2 for the smaller and larger objects, respectively, with the 2D-ASG for a medium contrast object (Fig. 6). The line profile at the bone soft tissue interface shows the edge blurring is significantly reduced with the clinical software correction and further reduced with the 2D-ASG (Supplementary Fig. S5).

4. Discussion

This investigation centered on two key aspects. Firstly, it aimed to assess the reliable integration of a 2D-ASG in a large SID, proton therapy gantry-mounted CBCT system. Secondly, it focused on studying how the proposed system could enhance the quality of CBCT images. By exploring these two areas, we aimed to determine both the feasibility of incorporating 2D-ASGs into existing setups and the potential improvements it could bring to CBCT imaging for IGPT.

While proton therapy gantry geometric accuracy and stability have been studied by others, these works did not focus on the effect of gantry stability on the 2D-ASG wall shadow properties and wall shadow suppression [35–37]. Although proton gantry flex affects the shape and position of the wall shadows, variations in wall shadow properties can be characterized as a function of gantry angle with high accuracy. Thus, in this work, wall shadows could be suppressed by using standard flat-field correction approaches [38]. From a qualitative point of view, the absence of ring artifacts in CBCT images indicates the efficacy of grid wall shadow suppression. Another critical point is the repeatability or temporal stability of 2D-ASG wall shadow characteristics. Changes in 2D-ASG wall shadow properties over time would lead to a mismatch in wall shadows in a patient's CBCT scan and calibration data, causing ring artifacts. The similarity in wall shadow properties of the gantry in data sets, taken 3 months apart indicates the highly repeatable nature of grid wall shadows and gantry flex characteristics over time. These observations imply that a single calibration data set, a flood field CBCT scan, can potentially correct the grid wall shadows in CBCT scans over extended periods. This work indicates that implementing a 2D-ASG in an extended SID proton therapy CBCT system is feasible. Notably, the influence of proton gantry flex on the correction of 2D-ASG's footprint was insignificant. Relatively larger voxel size in CBCT images might have also
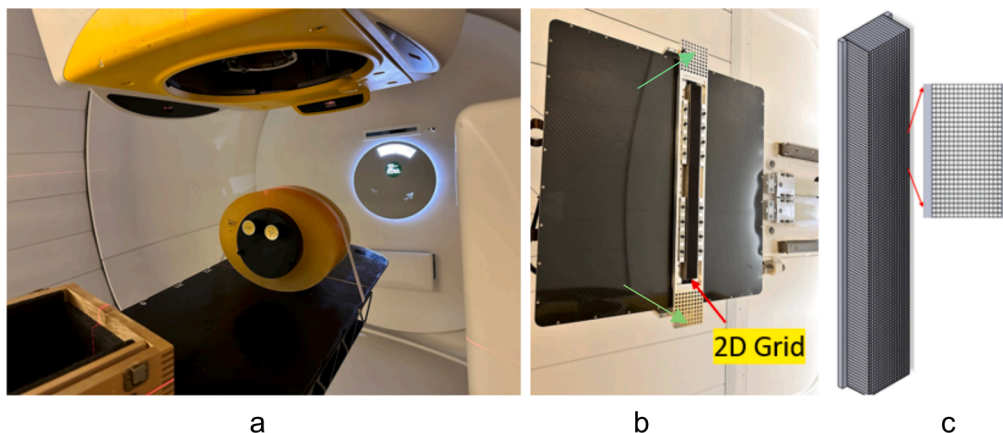

Fig. 1. (a) CBCT imaging setup in the IBA Proteus Plus gantry. (b) The custom 2D-ASG mounting platform that was integrated with the FPD. (c) Sketch of the 2D-ASG prototype with mounting flanges on both sides.
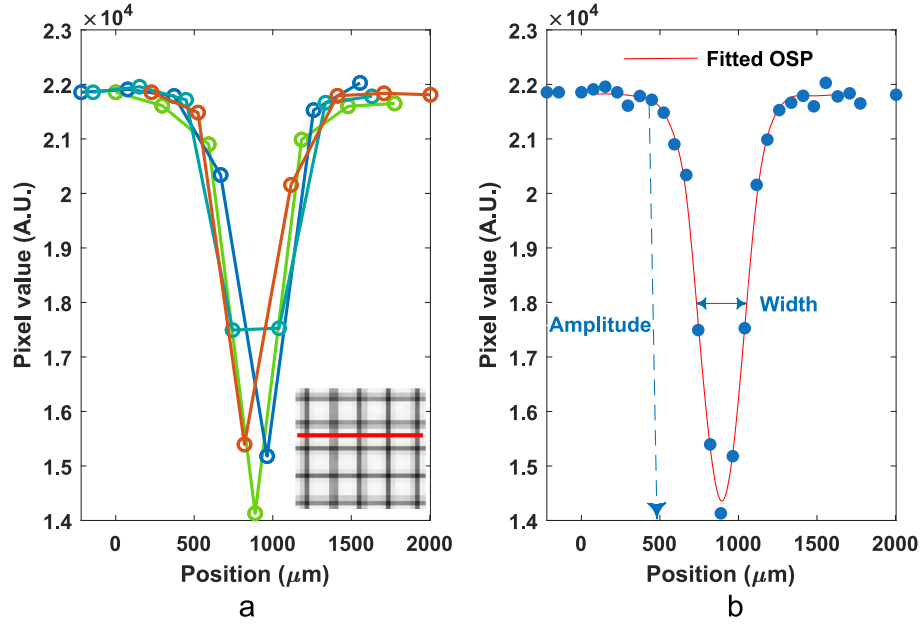
Fig. 2. (a) Vertical grid wall shadows from 5 adjacent grid walls are represented by different colors. Pixels in individual grid wall shadows were rearranged to generate the Oversampled Shadow Profile (OSP). (b) Rearrangement of pixel values in (a) yields the OSP, which characterizes the grid wall shadow. The left–right shift of the minimum of the OSP for OSPs acquired at different gantry angles characterizes the shift in grid line shadow position.
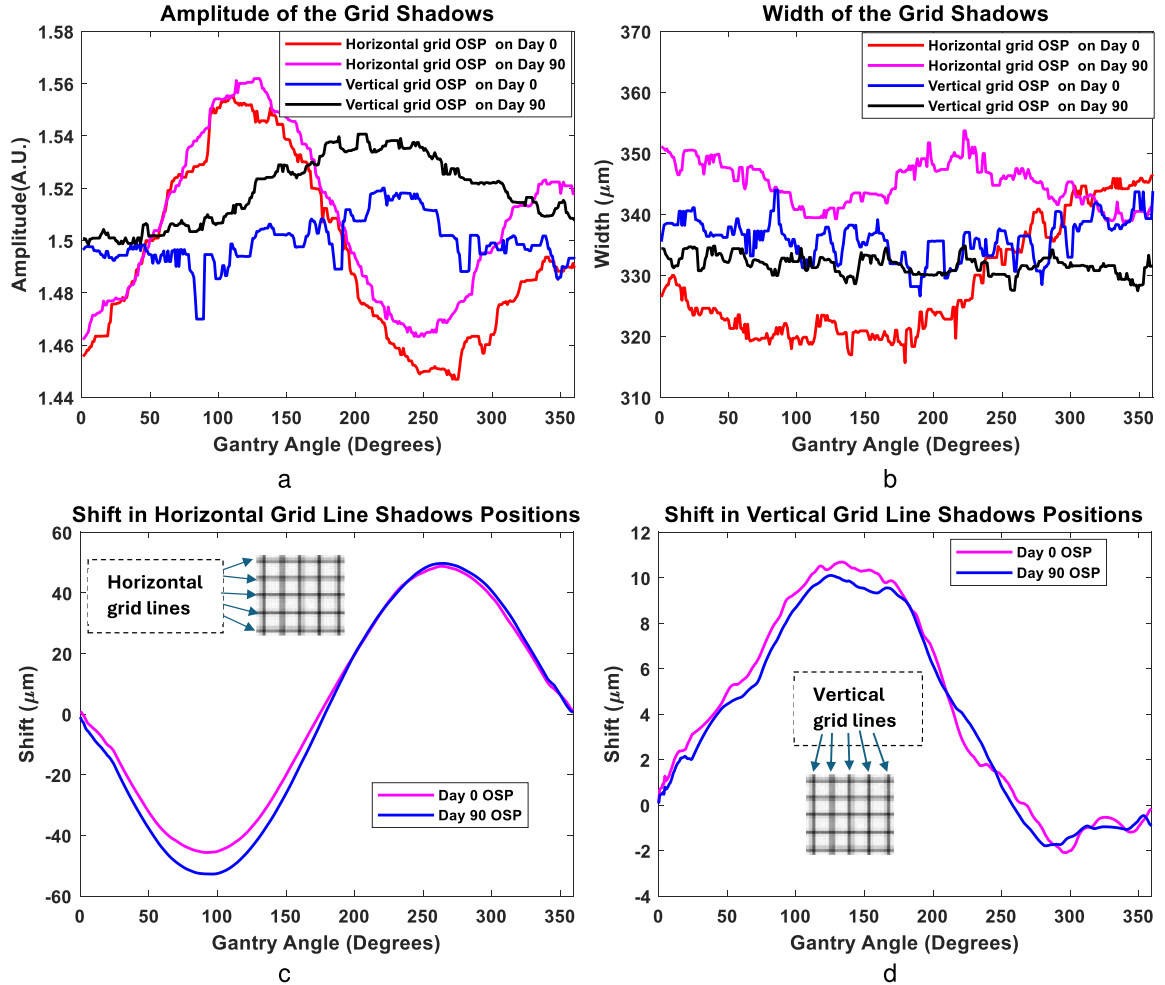

Fig. 3. Normalized amplitude and width of grid wall shadows as a function of gantry angle in two experiments performed three months apart are shown in (a) and (b), respectively. The shift in grid wall shadow positions as a function of gantry angle for horizontal and vertical grid walls are shown in (c) and (d), respectively.
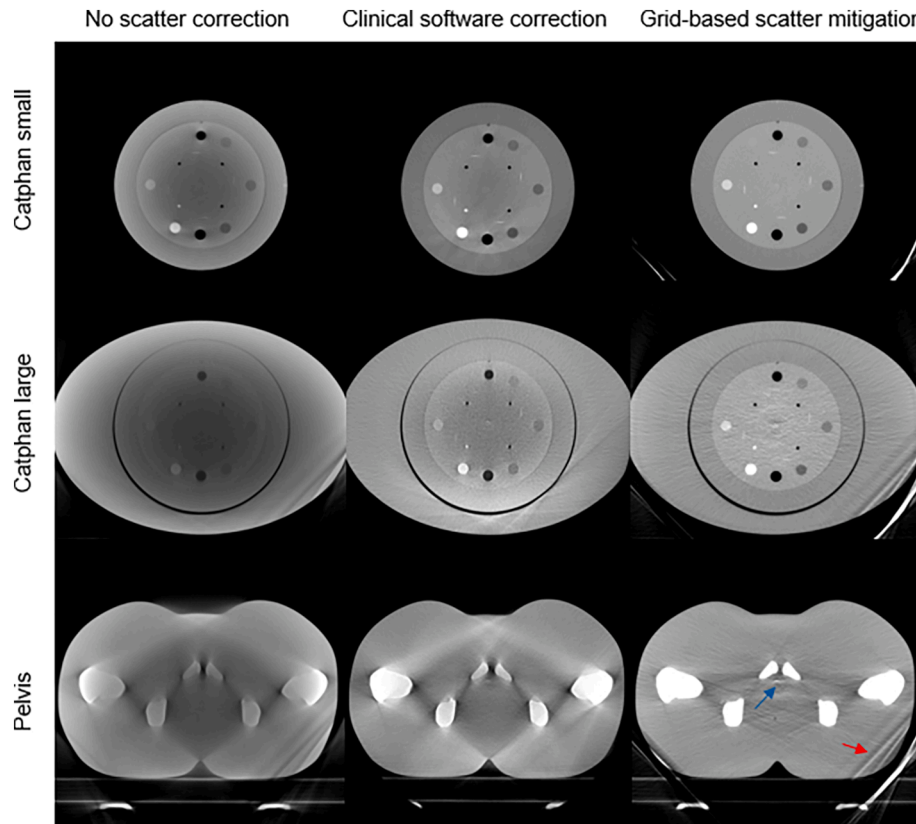
Fig. 4. CBCT slices of the Catphan, Catphan large, and Pelvis Phantoms without and with scatter correction using the clinical software, and with the 2D-ASG based scatter mitigation. The HU window is [-700, 300] and [-500, 500] for uncorrected and both the scatter corrected CBCT images. The ring artifact in the center of the CBCT images as pointed by a blue arrow was due to the junction of two grid modules. The artifact shown by red arrow is due to the gantry rolling floor truncating the field of view. This truncation was accounted by the Clinical Software, whereas it was not corrected in other images.
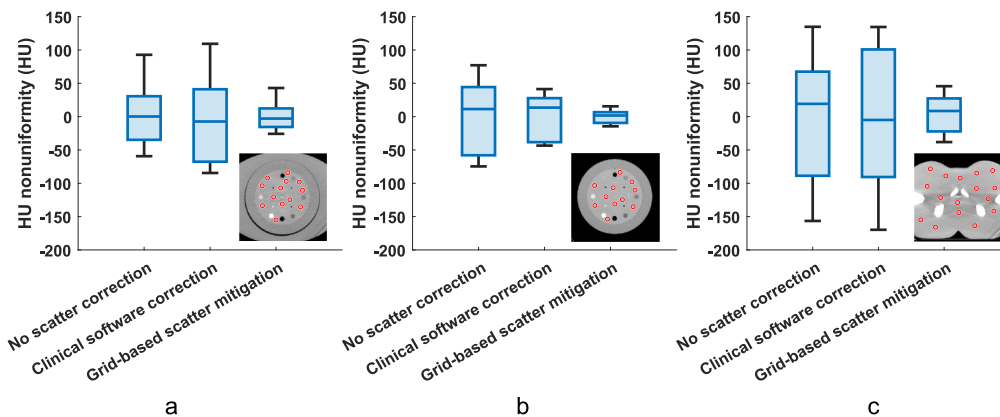

Fig. 5. Effect of HU nonuniformity and HU loss in the scatter uncorrected, clinical software corrected, and 2D-ASG based scatter mitigated CBCT images. (a) Catphan large with the annular ring, (b) Catphan small, and (c) Pelvis phantom. The box represents the upper and lower quartiles as the top and bottom edges of the box. The whiskers or lines that extend below and above the box represent the maximum and minimum HU nonuniformity. The line across the box is the median value.

reduced artifacts caused by the 2D-ASG's footprint.

While software-based scatter corrections also reduce HU degradation, image artifacts, and improve CNR [39,40], the 2D-ASG based scatter mitigation approach is an alternative to enhance the quality of CBCT images. As expected, there is a significant reduction in scatter-induced cupping and shading artifacts. While new artifacts were introduced due to the abutment of two grid modules, this issue could be addressed by developing a monolithic 2D-ASG, eliminating grid module abutment artifacts. HU accuracy and spatial uniformity among phantoms of different sizes and compositions were significantly improved by

using the 2D-ASG. While scatter fluence reduction, residual scatter correction, and primary reduction caused an increase in noise, CNR was enhanced by the 2D-ASG due to contrast enhancement. It is also important to note that CBCT images generated by the clinical software were based on the AdaptInsight 2.1 Software using an older calibration pipeline. Our future work will employ AdaptInsight 2.2 to improve the quality of CBCT images acquired without the 2D-ASG.

Such advancements in CBCT image quality, particularly in proton therapy, hold significant promises for enhancing treatment precision and dose delivery accuracy. Besides improving target localization,
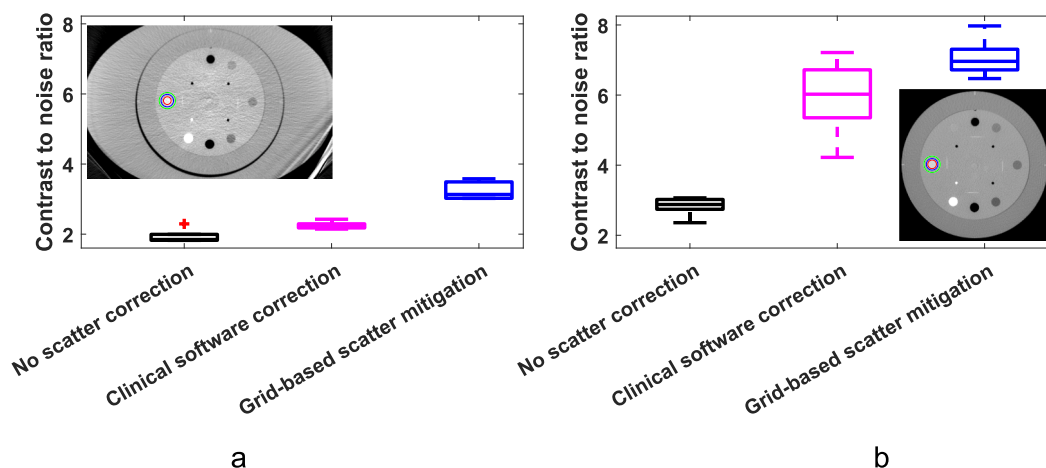
Fig. 6. (a) CNR of Delrin insert in Catphan large, (b) and Catphan small.

accurate CT numbers in CBCT images may enable the implementation of online dose calculations by directly employing the CBCT images, negating the need for CT number override or multi-detector row CT acquisition in the treatment vault [41,42]. Moreover, reducing scatter-induced artifacts and improving CNR may improve downstream automation processes in CBCT-based treatment plan adaptations, such as artificial intelligence-based structure segmentation in daily CBCT images.

In this study, the grid prototype was designed to have 2.7 cm width to reduce manufacturing costs, which limits the field of view in the cranio-caudal direction. In a clinical CBCT imaging scenario, the width of the 2D-ASG is expected to be much larger, such that it covers the entire area of the FPD. Another issue is the increased weight of the large-area 2D-ASG which may adversely affect the gantry and detector arm flex characteristics. This work indicates that the proton gantry and detector arm flex by itself is not prohibitive for 2D-ASG implementation. However, fabrication of a large width 2D-ASG, and the effect of its weight on gantry flex and image quality remain to be investigated. Besides scatter suppression, there are other preprocessing steps that impact CBCT image quality, such as beam hardening correction, lag correction, off-focal radiation correction, ring artifact correction. Such correction methods will be studied in the future.

Author contributions statement

Uttam Pyakurel: Algorithm development and optimization, image processing and reconstruction, analysis, interpretation of results, and writing the original draft.

Yawei Zhang: Experiment setup, data acquisition, interpretation of the results, review and editing of the manuscript.

Ryan Sabounchi: Experiment hardware development, fabrication, and testing, review and editing of the manuscript.

Farhang Bayat: Data correction algorithm development, review and editing of the manuscript.

Sébastien Brousmiche: Image reconstruction, data processing, interpretation of the results, review and editing of the manuscript.

Curtis Bryant: Provided resources for experiments, review and editing of the manuscript.

Nancy Mendenhall: Provided resources for experiments, review and editing of the manuscript.

Perry Johnson: Coordination of experiments, provided resources for experiments, review and editing of the manuscript.

Cem Altunbas: Secured funding, conceptualized, designed and supervised the project, analysis and interpretation of the results, writing, review and editing of the manuscript.

Declaration of competing interest

The authors declare the following financial interests/personal relationships which may be considered as potential competing interests: Sébastien Brousmiche is an employee of IBA. Cem Altunbas is the founder of M2 Technologies. Uttam Pyakurel, Yawei Zhang, Ryan Sabounchi, Farhang Bayat, Curtis Bryant, Nancy Mendenhall, Perry Johnson do not have any conflicts of interest.

Acknowledgements

Appendix A. Supplementary data

Supplementary data to this article can be found online at https://doi.org/10.1016/j.phro.2025.100730.

References

[1] Landry G, et al. Investigating CT to CBCT image registration for head and neck proton therapy as a tool for daily dose recalculation. Med Phys 2015;42:1354–66. https://doi.org/10.1118/1.4908223.

[2] Giacometti V, Hounsell AR, McGarry CK. A review of dose calculation approaches with cone beam CT in photon and proton therapy. Phys Medica 2020;76:243–76. https://doi.org/10.1016/j.ejmp.2020.06.017.

[3] Hua C, et al. A robotic C-arm cone beam CT system for image-guided proton therapy: design and performance. Br J Radiol 2017;90:20170266. https://doi.org/10.1259/bjr.20170266.

[4] Veiga C, et al. A comprehensive evaluation of the accuracy of CBCT and deformable registration based dose calculation in lung proton therapy. Biomed Phys Eng Express 2017;3:015003. https://doi.org/10.1088/2057-1976/3/1/015003.

[5] Jaffray DA, Siewerdsen JH, Wong JW, Martinez AA. Flat-panel cone-beam computed tomography for image-guided radiation therapy. Int J Radiat Oncol Biol Phys 2002;53:1337–49. https://doi.org/10.1016/S0360-3016(02)02884-5.

[6] Zhao W, Vernekohl D, Zhu J, Wang L, Xing L. A model-based scatter artifacts correction for cone beam CT. Med Phys 2016;43:1736–53. https://doi.org/10.1118/1.4943796.

[7] Wiegert J, Bertram M, Rose G, Aach T. Model based scatter correction for cone-beam computed tomography. Proc SPIE 2005;5745:271–82. https://doi.org/10.1117/12.594520.

[8] Lazos D, Williamson JF. Monte Carlo evaluation of scatter mitigation strategies in cone-beam CT. Med Phys 2010;37:5456–70. https://doi.org/10.1118/1.3488978.

[9] Bertram M, Sattel T, Hohmann S, Wiegert J. Monte-Carlo scatter correction for cone-beam computed tomography with limited scan field-of-view. Proc SPIE 2008; 6913:674–83. https://doi.org/10.1117/12.771103.

[10] Ruhrnschopf E-P, Klingenbeck K. A general framework and review of scatter correction methods in x-ray cone-beam computerized tomography. Part 1: scatter compensation approaches. Med Phys 2011;38:4296–311. https://doi.org/10.1118/1.3599033.

[11] Park YK, Sharp GC, Phillips J, Winey BA. Proton dose calculation on scatter-corrected CBCT image: feasibility study for adaptive proton therapy. Med Phys 2015;42:4449–59. https://doi.org/10.1118/1.4923179.

[12] Andersen AG, et al. Evaluation of an a priori scatter correction algorithm for cone-beam computed tomography based range and dose calculations in proton therapy. Phys Imaging Radiat Oncol 2020;16:89–94. https://doi.org/10.1016/j.phro.2020.09.014.

[13] Kurz C, et al. Investigating deformable image registration and scatter correction for CBCT-based dose calculation in adaptive IMPT. Med Phys 2016;43:5635–46. https://doi.org/10.1118/1.4962933.

[14] Bootsma G, Verhaegen F, Jaffray D. The effects of compensator and imaging geometry on the distribution of x-ray scatter in CBCT. Med Phys 2011;38:897–914. https://doi.org/10.1118/1.3539575.

[15] Zhang G, Marshall N, Jacobs R, Liu Q, Bosmans H. Bowtie filtration for dedicated cone beam CT of the head and neck: a simulation study. Br J Radiol 2013;86: 20130002. https://doi.org/10.1259/bjr.20130002.

[16] Zhu L, Xie Y, Wang J, Xing L. Scatter correction for cone-beam CT in radiation therapy. Med Phys 2009;36:2258–68. https://doi.org/10.1118/1.3130047.

[17] Liu X, Shaw CC, Wang T, Chen L, Altunbas MC, Kappadath SC. An accurate scatter measurement and correction technique for cone beam breast CT imaging using scanning sampled measurement (SSM) technique. Phys Med 2006;6142:1059–65. https://doi.org/10.1117/12.656655. SPIE.

[18] Zhu L, Bennett NR, Fahrig R. Scatter correction method for X-ray CT using primary modulation: theory and preliminary results. IEEE Trans Med Imaging 2006;25: 1573–87. https://doi.org/10.1109/TMI.2006.884636.

[19] Siewerdsen JH, Jaffray DA. Optimization of x-ray imaging geometry (with specific application to flat-panel cone-beam computed tomography). Med Phys 2000;27: 1903–14. https://doi.org/10.1118/1.1286590.

[20] Fetterly KA, Schueler BA. Experimental evaluation of fiber-interspaced antiscatter grids for large patient imaging with digital x-ray systems. Phys Med Biol 2007;52: 4863. https://doi.org/10.1088/0031-9155/52/16/010.

[21] Wiegert J, et al. Performance of standard fluoroscopy antiscatter grids in flat-detector-based cone-beam CT. Proc SPIE 2004;5368:67–78. https://doi.org/10.1117/12.535387.

[22] Altunbas C, Alexeev T, Miften M, Kavanagh B. Effect of grid geometry on the transmission properties of 2D grids for flat detectors in CBCT. Phys Med Biol 2019; 64:225006. https://doi.org/10.1088/1361-6560/ab4af4.

[23] Altunbas C, Kavanagh B, Alexeev T, Miften M. Transmission characteristics of a two dimensional antiscatter grid prototype for CBCT. Med Phys 2017;44:3952–64. https://doi.org/10.1002/mp.12346.

[24] Yu Z, Park Y, Altunbas C. Simultaneous scatter rejection and correction method using 2D antiscatter grids for CBCT. Proc SPIE 2020;11312:682–9. https://doi.org/10.1117/12.2549763.

[25] Altunbas C, Park Y, Yu Z, Gopal A. A unified scatter rejection and correction method for cone beam computed tomography. Med Phys 2021;48:1211–25. https://doi.org/10.1002/mp.14681.

[26] Bayat F, Ruan D, Miften M, Altunbas C. A quantitative CBCT pipeline based on 2D antiscatter grid and grid-based scatter sampling for image-guided radiation therapy. Med Phys 2023;50:7980–95. https://doi.org/10.1002/mp.16681.

[27] Bayat F, Eldib ME, Kavanagh B, Miften M, Altunbas C. Concurrent kilovoltage CBCT imaging and megavoltage beam delivery: suppression of cross-scatter with 2D antiscatter grids and grid-based scatter sampling. Phys Med Biol 2022;67: 165005. https://doi.org/10.1088/1361-6560/ac8268.

[28] Altunbas C. Feasibility of dual-energy CBCT material decomposition in the human torso with 2D anti-scatter grids and grid-based scatter sampling. Med Phys 2024; 51:334–47. https://doi.org/10.1002/mp.16611.

[29] Bayat F, et al. 2D antiscatter grid and scatter sampling based CBCT method for online dose calculations during CBCT guided radiation therapy of pelvis. Med Phys 2023;51:3053–66. https://doi.org/10.1002/mp.16867.

[30] Pyakurel U, Sabounchi R, Eldib M, Bayat F, Phan H, Altunbas C. Evaluation of a compact cone beam CT concept with high image fidelity for point-of-care brain imaging. Sci Rep 2024;14:28286. https://doi.org/10.1038/s41598-024-79874-2.

[31] Eldib ME, Bayat F, Miften M, Altunbas C. A simulation study to evaluate the effect of 2D antiscatter grid primary transmission on flat panel detector based CBCT image quality. Biomed Phys Eng Express 2023;9:065011. https://doi.org/10.1088/2057-1976/acfb8a.

[32] Altunbas C, Park Y, Yu Z, Gopal A. A unified scatter rejection and correction method for cone beam computed tomography. Med Phys 2021;48:1211–25. https://doi.org/10.1002/mp.14681.

[33] Rit S, Oliva MV, Brousmiche S, Labarbe R, Sarrut D, Sharp GC. The Reconstruction Toolkit (RTK), an open-source cone-beam CT reconstruction toolkit based on the Insight Toolkit (ITK). J Phys Conf Ser 2014;489:012079. https://doi.org/10.1088/1742-6596/489/1/012079.

[34] Catphan® 500 and 600 Manual. TPL 2013. https://static1.squarespace.com/static/5367b059e4b05a1adcd295c2/t/678e8e1baaff5463fb7fecb0/1737395740055/CTP500600ProductGuide20250120.pdf.

[35] Kato T, et al. End-to-end test to evaluate the comprehensive geometric accuracy of a proton rotating gantry using a cone-shaped scintillator screen detector. Radiol Phys Technol 2020;13:144–51. https://doi.org/10.1007/s12194-020-00562-7.

[36] Wang N, Ghebremedhin A, Patyal B. Commissioning of a proton gantry equipped with dual x-ray imagers and a robotic patient positioner, and evaluation of the accuracy of single-beam image registration for this system. Med Phys 2015;42: 2979–91. https://doi.org/10.1118/1.4921122.

[37] Zhu M, Botticello T, Lu HM, Winey B. Long-term stability and mechanical characteristics of kV digital imaging system for proton radiotherapy. Med Phys 2014;41:041706. https://doi.org/10.1118/1.4868460.

[38] Alexeev T, Kavanagh B, Miften M, Altunbas C. Two-dimensional antiscatter grid: a novel scatter rejection device for Cone-beam computed tomography. Med Phys 2018;45:529–34. https://doi.org/10.1002/mp.12724.

[39] Lalonde A, Winey B, Verburg J, Paganetti H, Sharp GC. Evaluation of CBCT scatter correction using deep convolutional neural networks for head and neck adaptive proton therapy. Phys Med Biol 2020;65:245022. https://doi.org/10.1088/1361-6560/ab9fcb.

[40] Nomura Y, Xu Q, Shirato H, Shimizu S, Xing L. Projection-domain scatter correction for cone beam computed tomography using a residual convolutional neural network. Med Phys 2019;46:3142–55. https://doi.org/10.1002/mp.13583.

[41] Taasti VT, Wohlfahrt P. From computed tomography innovation to routine clinical application in radiation oncology–a joint initiative of close collaboration. Phys Imaging Radiat Oncol 2024;29:100550. https://doi.org/10.1016/j.phro.2024.100550.

[42] Leibold D, Schaart DR, Goorden MC. Optimizing proton stopping power ratio prediction with dual-energy cone-beam CT using the Cramér-Rao lower bound. Proc SPIE 2024;12925:688–98. https://doi.org/10.1117/12.3006731.